Plume emission statistics in turbulent Rayleigh–Bénard convection

Erwin P. van der Poel[1,†], Roberto Verzicco[2,1], Siegfried Grossmann[3] and Detlef Lohse[1]

[1]Physics of Fluids group, Department of Science and Technology,
Mesa+ Institute and J.M. Burgers Centre of Fluid Dynamics, University of Twente,
PO Box 217, 7500 AE Enschede, The Netherlands

[2]Dipartimento di Ingegneria Industriale, University of Rome 'Tor Vergata', Via del Politecnico 1,
Roma 00133, Italy

[3]Fachbereich Physik, Philipps-Universität Marburg, Renthof 6, D-35032 Marburg, Germany

Direct numerical simulations (DNS) of turbulent thermal convection in a $Pr = 0.7$ fluid up to $Ra = 10^{12}$ are used to study the statistics of thermal plumes. At various vertical locations in a cylindrical set-up with aspect ratio $\Gamma = \text{width/height} = 1/3$, plumes are identified and their properties extracted. It is found that plumes are much less likely to be emitted from plate regions with large wind shear. Close to the plates, the plumes have a unimodal log–normal distribution, whereas at more central locations the distribution becomes weakly bimodal, which can be traced back to clustering of the plumes and influence of the large-scale circulation. The number of hot plumes decreases with height. The width of the plumes scales with Ra approximately as Nu^{-1}, indicating that it is determined by the thermal boundary layer thickness.

Key words: Bénard convection, plumes/thermals, turbulent convection

1. Introduction

Rayleigh–Bénard (RB) convection (Ahlers, Grossmann & Lohse 2009; Lohse & Xia 2010; Chillà & Schumacher 2012) is a system in which a fluid is heated from below and cooled from above and convection arises due to the density differences induced by the different temperatures. This system is used to model natural convection, preserving most of the relevant phenomena while reducing the complexity of the problem. As is commonly done and well justified, we adopt the Boussinesq approximation, i.e. the fluid properties are assumed to be independent of the temperature except in the buoyancy term of the momentum equation.

RB convection features ubiquitous coherent structures, which continue to survive in strong turbulence. The most prevalent structures are thermal plumes and large-scale circulation (LSC). The thermal plumes and LSC are intrinsically coupled (Grossmann & Lohse 2004), as thermal plumes cluster to form a LSC (Parodi *et al.* 2004; Xi, Lam & Xia 2004) and fragment in the bulk (Bosbach, Weiss & Ahlers 2012). In addition, both thermal and shear instabilities can result in the emission of buoyant fluid parcels,

† Email address for correspondence: e.p.vanderpoel@utwente.nl

as was shown by Hunt *et al.* (2003), who distinguished between plumes and puffs. Here this distinction is not made, and all buoyant parcels are classified as plumes, irrespective of the mechanism behind their origin. Zhou, Sun & Xia (2007) divided the plumes into 'sheet' or 'line' plumes of elongated shape and circular 'mushroom' plumes. They showed that the plumes are predominantly sheetlike close to the plates and mushroomlike higher in the system. Eventually the numbers of both types of plumes are shown to decrease with height. We will connect this phenomenon to the clustering of plumes by using a plume identification criterion and image segmentation.

The concept of thermal plumes has been used to directly and indirectly derive scaling laws for the heat flux by Castaing *et al.* (1989) and Grossmann & Lohse (2004), respectively. This is because the contribution of thermal plumes to the total heat flux, relative to that of the LSC, is substantial (Belmonte, Tilgner & Libchaber 1993). It is generally assumed that thermal plumes have a characteristic width equal to that of the thermal boundary layer, which stems from the understanding that thermal plumes are detached thermal boundary layers. This assumption is used by Castaing *et al.* (1989) and Grossmann & Lohse (2004) to derive scaling laws for the heat flux through the system. We attempt to extract the plume width and thereby substantiate this assumption.

The dynamics of plumes is complex. Plumes move not only vertically but also horizontally, being advected by the LSC, as was observed by Sano, Wu & Libchaber (1989). In addition, the dynamics of the LSC is highly non-trivial (Brown, Nikolaenko & Ahlers 2005; Ahlers *et al.* 2009; Sugiyama *et al.* 2010), affecting the collective motion of the thermal plumes through an opposing pressure gradient. This complicates the simple (two-dimensional) picture of a stationary LSC with thermal plumes moving alongside it that was sketched by Kadanoff (2001) (see figure 1), as Ching *et al.* (2004) and Emran & Schumacher (2012) have shown that plumes are found in the centre of the cell and even throughout the entire volume. Recently, Ostilla-Mónico *et al.* (2014) found in a Taylor–Couette (TC) flow that the boundary layer transition from laminar to turbulent occurs in plume-ejecting locations at lower driving than in the wind-sheared region. It was shown by Eckhardt, Grossmann & Lohse (2007) that RB is analogous to TC, which raises the question of whether this phenomenon can also be observed in RB. Because the driving in RB is less efficient than in TC, turbulent boundary layers, such as those seen in RB by Ahlers *et al.* (2012), are difficult to observe due to the required high *Ra* and long averaging time. This prevents a study in RB convection comparable to the TC flow study by Ostilla-Mónico *et al.* (2014). However, it is possible to study the connection between wind shear and plume ejection and hence gain insights into how shear is related to thermal plumes and in turn to boundary layer turbulence. The turbulent boundary layer in RB is an important ingredient in expected heat flux scaling arguments by Kraichnan (1962) and Grossmann & Lohse (2011) for the ultimate regime.

2. Method

Direct numerical simulations (DNS) of the Boussinesq equations were performed using a second-order staggered finite difference scheme by Verzicco & Camussi (1999, 2003) that is energy conserving. The governing equations in dimensionless form are

$$\partial_t u_i + u_j \partial_j u_i = -\partial_i p + \sqrt{\frac{Pr}{Ra}}\, \partial_j^2 u_i + \theta \delta_{i3}, \qquad (2.1)$$

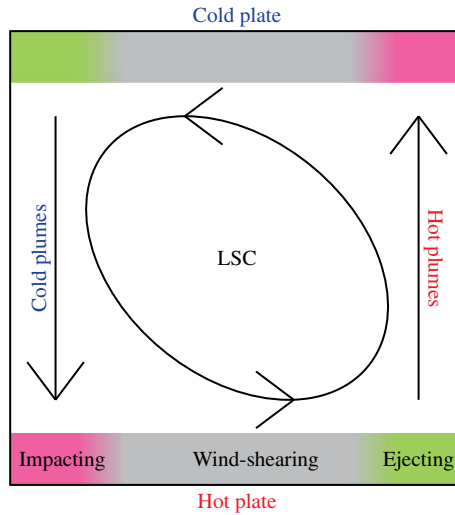$$\partial_t \theta + u_j \partial_j \theta = \frac{1}{\sqrt{Ra\, Pr}}\, \partial_j^2 \theta, \qquad (2.2)$$

FIGURE 1. (Colour online) Sketch of a confined Rayleigh–Bénard system with $\Gamma \approx 1$. A large-scale circulation and plume paths are indicated, as well as the positions of the three different horizontal boundary regions: impacting, wind-shearing and ejecting. The corner rolls are not shown.

where $\hat{\boldsymbol{e}}_3$ is the unit vector that is antiparallel to gravity, u_i is the velocity normalized by the free-fall velocity $\sqrt{g\beta\Delta L}$, t is the time normalized by the free-fall time $\sqrt{L/(g\beta\Delta)}$ and θ is the temperature normalized by Δ, the temperature difference between the top and bottom plates. The control parameters of the system are the non-dimensional temperature difference, i.e. the Rayleigh number $Ra = g\beta\Delta L^3/(\nu\kappa)$, the Prandtl number $Pr = \nu/\kappa$ of the fluid and the aspect ratio $\Gamma = D/L$, where L is the height of the sample and D is its width, g is the gravitational acceleration, β is the thermal expansion coefficient, ν is the kinematic viscosity and κ is the thermal diffusivity. The boundary conditions chosen are no-slip conditions on all walls for the velocity, adiabatic conditions on the sidewall and isothermal conditions on the horizontal plates for temperature. The numerical set-up has a Prandtl number of $Pr = 0.7$ and an aspect ratio of $\Gamma = 1/3$. In addition, for fixed Ra, a low-aspect-ratio domain is computationally less demanding than a large-aspect-ratio domain due to the smaller volume. The resolutions used are up to $1536 \times 512 \times 2048$ for Rayleigh number $Ra = 10^{12}$ with clustering of grid points near the boundaries similar to the previous high-Ra DNS of Stevens, Lohse & Verzicco (2011). The Nusselt number Nu, which quantifies the area-averaged heat flux, is calculated as both an area average of the convective term, $Nu = \sqrt{Ra\,Pr}\,\langle u_z\theta\rangle_{r,\phi,t} + 1$, and a line average on the horizontal plates of the diffusive term, $Nu = -\langle\partial_z\theta|_{z=0,L}\rangle_{r,\phi,t}$. We verify these results for Nu by also calculating Nu through the kinetic and thermal dissipation rates (Shraiman & Siggia 1990; Siggia 1994). Horizontal cross-sections of $u_{r,\phi,z}(r, \phi)$ and $\theta(r, \phi)$ are used that have a time interval of 0.5 free-fall time. This interval is tested for statistical independence and shown to be sufficient. The number of cross-sections required for statistical convergence is approximately 100.

Figure 2 shows the compensated Nu as a function of Ra compared with previous results obtained at $\Gamma = 1/2$. It is apparent that the heat fluxes for $\Gamma = 1/3$ and $\Gamma = 1/2$ are within the error bars of the data. In addition, no transition in the $Nu(Ra)$ scaling
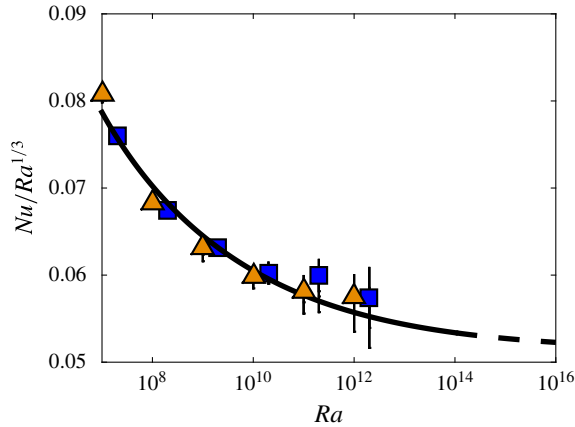
FIGURE 2. (Colour online) Compensated Nusselt number $Nu/Ra^{1/3}$ as a function of Ra. The blue squares indicate the DNS data for $\Gamma = 1/2$ of Stevens *et al.* (2011); the data used in this paper for $\Gamma = 1/3$ is represented by the orange triangles; the solid black curve is the result of the Grossmann–Lohse fit for $Pr = 0.7$ from Stevens *et al.* (2013).

towards the steeper scaling (the so-called ultimate regime) is observed, and the system can be considered to be in the classical regime, i.e. the boundary layers are not yet turbulent, consistent with the theoretical expectation at $Ra \leqslant 10^{12}$ (Grossmann & Lohse 2000, 2001, 2011; Stevens *et al.* 2013).

Various methods for detecting plumes have been used previously, as reviewed by Ching *et al.* (2004). We define a thermal plume as the set of coordinates P where $\theta(r, \phi) - \langle\theta\rangle_{r,\phi} > c\theta_{RMS}$ and $\sqrt{Ra\,Pr}\,u_z(r, \phi)\theta(r, \phi) > c\,Nu$, as Huang *et al.* (2013) did in their study on confined RB convection. This criterion selects coordinates based on a high temperature anomaly and an excess of convective heat flux. Only hot plumes in the lower half of the domain are considered. The empirical constant c was chosen to be 0.8 in Huang *et al.* (2013), but here we take $c = 1.2$ to better separate the plumes from the background and emphasize their core structure. In addition, this choice of c matches the absolute value of the plume with the thermal boundary layer thickness, as will become apparent later on. A similar threshold based only on $u_z\theta$ was used by Emran & Schumacher (2012), where they found no qualitative differences in their results when the threshold was varied by two orders of magnitude. Along the lines of what was already shown there, quantitatively our results do depend on the value of threshold c. In figure 3(*d–f*) the results of applying this criterion to the temperature snapshots shown in figure 3(*a–c*) are depicted. It should be noted that this method of extracting thermal plume information limits the analysis to treating the plume as a two-dimensional entity, although in reality it is three-dimensional.

3. Plume size as a function of vertical position

Previous studies have revealed a log–normal distribution for the area of the plume (Zhou *et al.* 2007), for the length of the plumes (Bosbach *et al.* 2012) and for the spacing between the plumes (Puthenveettil & Arakeri 2005). These results suggest that the three quantities are intrinsically related to each other. The log–normal distribution suggests a fragmentation process that can be dealt with by the central limit theorem. The physical mechanism resulting in this distribution is that the fluctuations, acting
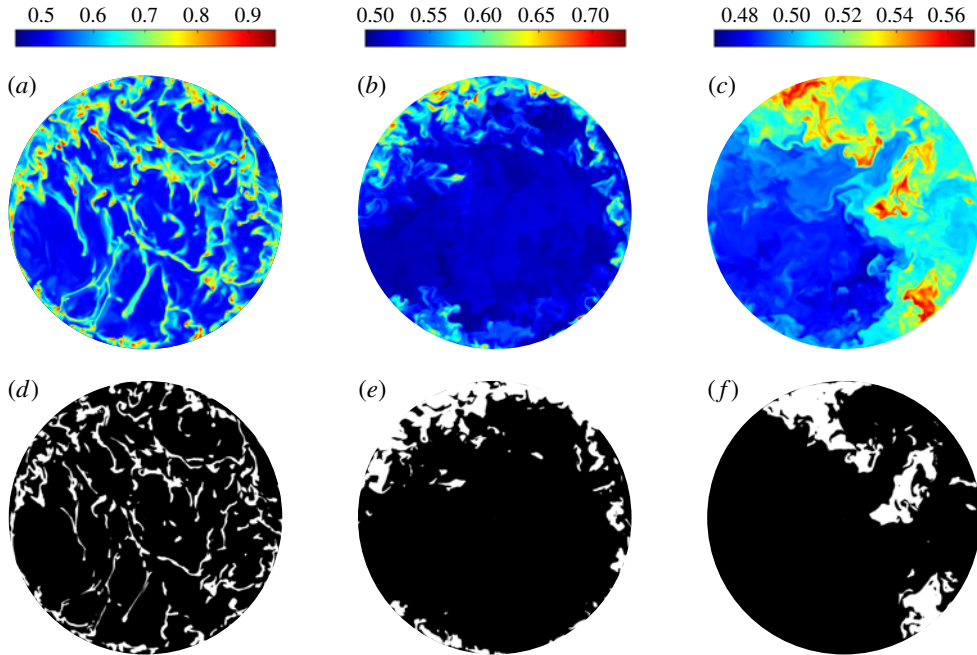
FIGURE 3. Temperature field snapshots for $Ra = 10^{11}$ at (*a*) $z/L = 0.004$, (*b*) $z/L = 0.04$ and (*c*) $z/L = 0.2$; hot and cold are indicated by red and blue, respectively, with colour maps displayed above the corresponding snapshots. Detection of thermal plumes P corresponding to the temperature field snapshots in (*a*)–(*c*) are shown in (*d*)–(*f*), respectively, where white indicates a plume.

on all scales, fragment the plumes (Zhou & Xia 2010). When modelling this process, the fragmentations are iterated, and a new sample is drawn from some distribution at each individual fragmentation. After many of these iterations, in each of which the plume area is always subdivided, a log–normal distribution results. We use the data at $Ra = 10^{11}$ to analyse the resulting plume area distribution as a function of z, because this gives the optimum available Ra with respect to minimum sidewall influence and the amount of statistics collected.

In figure 4(*a*) we plot the probability density functions of the plume areas at three vertical locations for $Ra = 10^{11}$. Closest to the plate, the distribution is unimodal and log–normal, which is illustrated by the quite accurate Gaussian fit to the data in the semi-log plot. Higher in the cell, the distribution becomes weakly bimodal. We interpret the second mode, indicating a larger plume area, as a reflection of plume clustering, which is a signature of the LSC, as the large-scale roll contains clusters of hot plumes in its upwelling region. The small area peaks indicate the existence of fragmented smaller plumes traversing the bulk. This view is supported by the data displayed in figure 4(*b*), where the most probable area is plotted as a function of the vertical location z. For all z, the most probable area is characterized by the smaller plumes, as in all of these bimodal distributions at $Ra = 10^{11}$ the right peak is considerably smaller than the left one. In figure 4(*b*) the thermal boundary layer thickness λ_θ based on the time- and volume-averaged Nu is shown. It can be seen that for $Ra = 10^{11}$ there is a region, extending much beyond λ_θ, where the most probable area is nearly constant. Beyond that region, the area of the small plumes
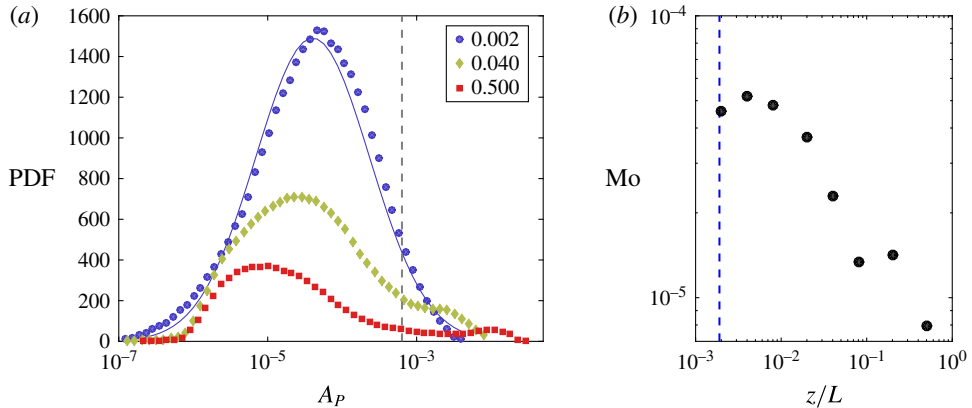
FIGURE 4. (Colour online) (*a*) Probability density functions (PDF) of the plume areas A_P (normalized by the total area) at different vertical locations z indicated in the legend for $Ra = 10^{11}$; the solid curve is a log–normal fit to the data at $z/L = 0.002$, and the grey dashed line indicates the characteristic plume area A_c. (*b*) The most probable value (Mo) of the PDF at each of the measured z values; the blue dashed line indicates the mean thermal boundary layer thickness $\lambda_\theta = 1/(2Nu)$.

decreases with height, a reflection of the fact that thermal plumes dissipate most of their energy near the plates (Kaczorowski & Wagner 2009) and are weakened through molecular and turbulent diffusion while moving towards the bulk of the flow higher in the cell (Tilgner, Belmonte & Libchaber 1993). The small plumes either become smaller or cluster to become part of the LSC, thus driving it.

The clustering is further highlighted by the behaviour of the plume number N_p as a function of height z, plotted in figure 5(*a*). It can be seen that N_p decreases strongly with z in the bulk, indicating the clustering and dissipation of plumes. In addition, there appears to be a region close to the lower boundary where N_p is approximately constant. The vertical extent of this region decreases with Ra, which signifies the relation of this region to the boundary layer thickness. Close to the upper boundary, N_p displays a steep drop-off, the location of which depends on Ra: the hot plumes travel further in the vertical direction for higher Ra. In figure 5(*b*), the normalized N_p' is plotted as function of z/λ_θ. Here N_p' is the number of plumes normalized by N_p at $z/\lambda_\theta = 4.5$. The profiles for $Ra = 10^{11}$ and $Ra = 10^{12}$ look strikingly similar, hinting at a universal profile for high Ra.

4. Scaling of the plume width with *Ra*

One could think of two parameters that determine the area of a plume. Close to the plates and thus for line plumes, the length of the plumes should be determined by the domain width $D = L\Gamma$, while their thickness is determined by the width λ_θ of the thermal boundary layer, characterized by $\lambda_\theta = L/(2Nu)$. The resulting characteristic non-dimensional plume area is then $A_c = L\Gamma/(2Nu)$. Illustratively, A_c is the area of a plume that is as long as the diameter of the cell and as wide as the thermal boundary layer. This characteristic plume area is indicated in figure 4(*a*). It can be seen that most of the plume areas are smaller than A_c; either the plume length, the plume width or both can differ from the dimensional expectation. Conceptually, the line plumes can be understood as detached thermal boundary layers of similar width; cf. Grossmann
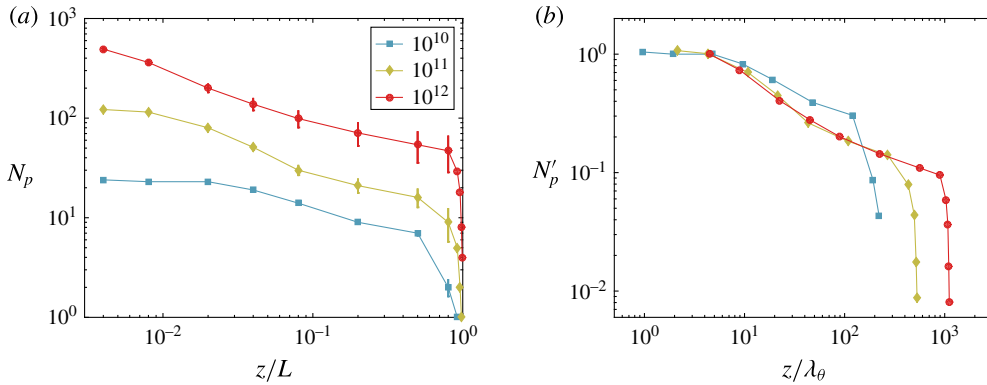
FIGURE 5. (Colour online) (*a*) The number N_p of hot plumes plotted as a function of height z/L for $Ra = 10^{10}$, 10^{11} and 10^{12}; the error bars increase with increasing height but are omitted from the last few data points for clarity. (*b*) The normalized number of plumes, N_p', plotted as a function of z/λ_θ, where N_p' is the number of plumes normalized by N_p at $z/\lambda_\theta = 4.5$.

& Lohse (2000). This has also been observed by Shishkina & Wagner (2008) using a different method. We expect that the observation that A_c approximately separates the two distributions at higher z/L is coincidental, as the assumptions associated with the definition of A_c are not applicable to plumes at this height.

As the absolute value of a quantity obtained from any thermal plume identification depends on the threshold, we compare the scaling of the width with the scaling of *Nu*. To be more precise, we compare the plume width with the thermal boundary layer thickness λ_θ, which scales approximately as $\lambda_\theta/L \sim Ra^{-0.31}$ for the data points $Ra = 10^9$, 10^{10} and 10^{11}. The data for $Ra = 10^{12}$ are not used in this analysis due to lack of statistical convergence.

The data at $z/L = 0.002$ are inside (for $Ra = 10^9$ and $Ra = 10^{10}$) or on the edge (for $Ra = 10^{11}$) of the thermal boundary layer. It is non-trivial to extract the width of the plumes from the results of the plume detection method used, as displayed in figure 3(*d*). We obtain the average plume width W_P by defining $\mathscr{D}$ as a so-called distance transform on *P* and $\mathscr{T}$ as a so-called thinning operation on *P*. These are defined as follows. For every plume element, the distance transform $\mathscr{D}$ gives the Euclidean distance to the closest non-plume element (figure 7*b*); the thinning operation $\mathscr{T}$ reduces *P* to minimally connected lines (figure 7*a*). These minimally connected lines are set to 1 and the rest of $\mathscr{T}$ is set to zero. The resulting set characterizes the 'backbone' of the plume. The plume width is obtained from $W_P = 2\langle(\mathscr{D} : \mathscr{T})/(\mathscr{T} : \mathscr{T})\rangle_t$, where $\mathscr{D} : \mathscr{T}$ denotes the componentwise inner product of $\mathscr{D}$ and $\mathscr{T}$, namely $\sum_{i,j} \mathscr{D}_{ij}\mathscr{T}_{ij}$ with the sum $\sum_{i,j}$ taken over all points of the set *P*. An alternative approach that gives identical results involves iterating over all the coordinates in $\mathscr{T}$ and time-averaging the minimum distance to the edge of a plume in *P*, which is more intuitive but much slower computationally.

The data are obtained at absolute vertical positions, constant for each *Ra* value. Consequently, the vertical position relative to the boundary layer thickness varies, as the boundary layer thickness decreases with *Ra*. In figure 4(*b*) we see that the most probable plume area can be approximated as constant between $z/L = 10^{-3}$ and 10^{-2}, revealing insensitivity to the vertical position over a substantial range. However,
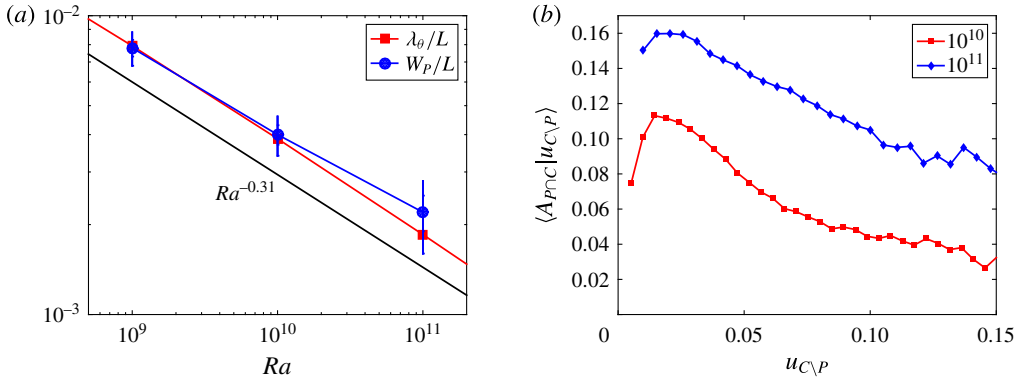
FIGURE 6. (Colour online) (*a*) Thermal boundary layer thickness $\lambda_\theta/L = 1/(2Nu)$ and plume thickness W_P, as defined in the text, plotted as functions of Ra; the solid black line represents $Ra^{-0.31}$, where the exponent is obtained from a fit to the λ_θ points. (*b*) Mean plume area inside the sliding window conditioned on the shear velocity outside the plume, $\langle A_{P \cap C} \mid u_{C \setminus P} \rangle$, for two values of Ra.

this insensitivity is only for the plume area and not for the plume width. Therefore, performing the analysis at a fixed vertical position introduces an uncertainty that is added to the data. The uncertainty is obtained from the variation of the plume width between $z/L = 0.002$ and 0.004 and is included in the error bar on each data point in figure 6(*a*), where the results of the plume width quantification are shown. The results demonstrate that the scaling of W_P is similar to the scaling of λ_θ. We emphasize that the close similarity of the absolute values is incidental, as the absolute value of W_P depends on c. On the other hand, this shows that $c = 1.2$ is a reasonable value for c. The scaling of W_P agrees approximately with that of λ_θ, which shows that the method used for plume identification provides the expected results and that it is the length of the plumes that gives rise to the deviations from A_c as a characteristic plume area.

5. Relation between wind shear and plume emission locations

The boundary layer of RB convection can conceptually be divided into three regions, namely the ejecting, wind-shearing and impacting regions, as Ostilla-Mónico *et al.* (2014) has shown for TC flow, which has similar topology. We refer to figure 1 for an indication of these regions in RB convection. In the ejecting region, the plumes are emitted from the corresponding boundary layer, whereas in the impacting regions, the descending current and thermal plumes originating from the opposite boundary impact the boundary layer under consideration. Between these two regions is the wind-shearing region, where the large-scale wind shear is high and the velocity is predominantly horizontal. In TC flow, Ostilla-Mónico *et al.* (2014) used this classification to rationalize the different boundary layer profiles found in each of these regions. As the ejecting region is defined by the emission of a large number of thermal plumes and the wind-shearing region is defined by high shear, this classification implies that regions of high shear emit fewer plumes than regions with low shear. This is opposite to what is observed in pressure-driven flows, where it is the high shear that results in bursts of momentum, concentration or temperature being emitted from the boundary layer into the bulk. This effect of plume emission
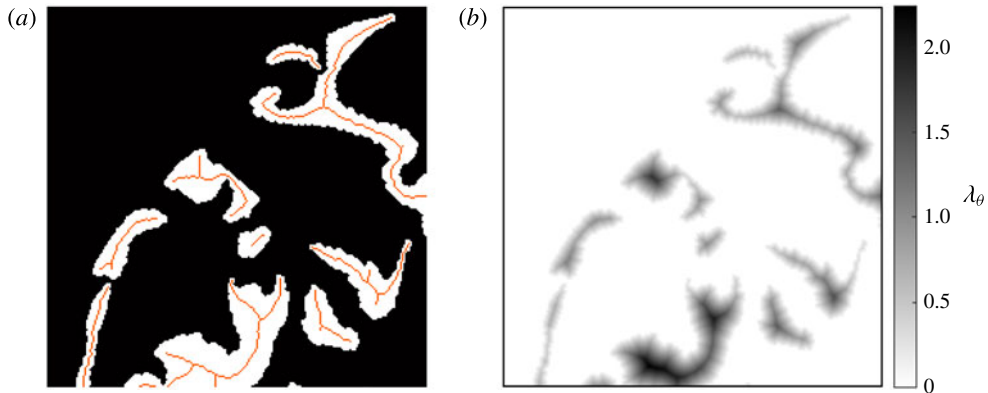
FIGURE 7. (Colour online) (*a*) Thinning operation $\mathscr{T}$, indicated by the thin lines, on an arbitrary subset of the domain at $z/L = 0.004$; here $\mathscr{T}$ is drawn on P for clarity, and we emphasize that $\mathscr{T}$ equals 1 on the thin lines and 0 elsewhere. (*b*) Distance function $\mathscr{D}$ on the same subset as in (*a*); the dark shading inside the plumes reflects the distance of the location to the edge of the plume in units of λ_θ.

being anticorrelated with large shear will now be quantified using our numerical data. A circle C with diameter $D_c = 0.05\,L\Gamma$ is used as a non-overlapping sliding window in which the mean shear velocity outside a plume, $u_{C\backslash P} = \langle\sqrt{(u_\phi^2 + u_r^2)}\rangle_{C\backslash P}$, and the plume area in that circle, $A_{P\cap C}$, are calculated. The velocity and area are normalized with the free-fall velocity and total area, respectively. For the shear velocity, only the area in the circle outside of the plume is considered, to avoid the contribution that the plume makes to the shear. We focus on the effect of the large-scale flow on the plumes by considering only the shear outside of a plume in the circle average. One of the contributions is the horizontal inflow near the boundary due to continuity. Conditioning $A_{P\cap C}$ on $u_{C\backslash P}$ gives $\langle A_{P\cap C}\,|\,u_{C\backslash P}\rangle$ averaged over r, ϕ and t, a quantity that can be used to quantify and study the effect of shear on plume emission. We find that only the amplitude of $\langle A_{P\cap C}\,|\,u_{C\backslash P}\rangle$ depends on D_c; in contrast, the trend does not, as long as $1 \gg D_c/\Gamma \gg 1/(2Nu)$. The analysis is performed on the data at $z/L = 0.002$, which is inside or on the edge of the viscous boundary layer for $Ra = 10^{10}$ and 10^{11}. At this height, the horizontal velocity can be interpreted as being proportional to the vertical gradient of horizontal velocity, averaged over $0 \leqslant z/L \leqslant 0.002$. In figure 6(*b*), the quantity $\langle A_{P\cap C}\,|\,u_{C\backslash P}\rangle$ is plotted for these two values of *Ra*. The trend is clear: regions of the boundary layer where the large-scale shear is high emit fewer plumes than regions where the shear is low. We emphasize that this analysis only accounts for the emitted plumes; plumes originating from the opposing plate that impact the boundary layer may display different behaviour, although we expect the behaviour to be similar.

6. Summary

In summary, we have studied three-dimensional thermal plumes using their cross-sections with horizontal planes at different heights in a cylindrical RB system. We have shown that the log–normal distribution of the thermal plume areas becomes weakly bimodal at higher vertical locations. This observation, together with the decline in the number of plumes, shows that there is clustering of plumes not only during a

transient, as was studied by Parodi *et al.* (2004), but also in a statistically stationary state. In addition, the weakly bimodal distribution indicates that plumes either cluster or lose energy while traversing the system. Both these mechanisms result in the number of plumes decreasing with increasing vertical position, an observation noted here and previously by Zhou *et al.* (2007). As was used in scaling law derivations by Castaing *et al.* (1989) and Grossmann & Lohse (2004), the assumption that the width of the plumes close to the plates is determined by the thermal boundary layer thickness is shown to be reasonable. The length of the plumes is not simply determined by the domain size; it originates from the flow structure and from the instability mechanism (Bosbach *et al.* 2012). The plumes are more likely to be emitted in regions of low shear, an observation used by Ostilla-Mónico *et al.* (2014) in TC flow to study the transition into turbulence of the boundary layers. The turbulent boundary layer is an important ingredient in the asymptotic scaling laws of Kraichnan (1962) and Grossmann & Lohse (2011), and our finding supports the classification of different horizontal regions of the boundary layer into ejecting, wind-shearing and impacting regions in RB convection as well. It provides an argument for conceptually dividing the RB cell not only vertically into bulk and boundary layer regions, but also horizontally into the aforementioned three regions. The existence of different boundary layer properties in these regions and their relative sizes can play an important role in understanding the transition to the ultimate regime in RB convection.

Acknowledgements

REFERENCES

AHLERS, G., BODENSCHATZ, E., FUNFSCHILLING, D., GROSSMANN, S., HE, X., LOHSE, D., STEVENS, R. J. A. M. & VERZICCO, R. 2012 Logarithmic temperature profiles in turbulent Rayleigh–Bénard convection. *Phys. Rev. Lett.* **109**, 114501.

AHLERS, G., GROSSMANN, S. & LOHSE, D. 2009 Heat transfer and large scale dynamics in turbulent Rayleigh–Bénard convection. *Rev. Mod. Phys.* **81**, 503.

BELMONTE, A., TILGNER, A. & LIBCHABER, A. 1993 Boundary layer length scales in thermal turbulence. *Phys. Rev. Lett.* **70**, 4067–4070.

BOSBACH, J., WEISS, S. & AHLERS, G. 2012 Plume fragmentation by bulk interactions in turbulent Rayleigh–Bénard convection. *Phys. Rev. Lett.* **108**, 054501.

BROWN, E., NIKOLAENKO, A. & AHLERS, G. 2005 Reorientation of the large-scale circulation in turbulent Rayleigh–Bénard convection. *Phys. Rev. Lett.* **95**, 084503.

CASTAING, B., GUNARATNE, G., HESLOT, F., KADANOFF, L., LIBCHABER, A., THOMAE, S., WU, X. Z., ZALESKI, S. & ZANETTI, G. 1989 Scaling of hard thermal turbulence in Rayleigh–Bénard convection. *J. Fluid Mech.* **204**, 1–30.

CHILLÀ, F. & SCHUMACHER, J. 2012 New perspectives in turbulent Rayleigh–Bénard convection. *Eur. Phys. J.* E **35**, 58.

CHING, E. S. C., GUO, H., SHANG, X. D., TONG, P. & XIA, K.-Q. 2004 Extraction of plumes in turbulent thermal convection. *Phys. Rev. Lett.* **93**, 124501.

ECKHARDT, B., GROSSMANN, S. & LOHSE, D. 2007 Torque scaling in turbulent Taylor–Couette flow between independently rotating cylinders. *J. Fluid Mech.* **581**, 221–250.

EMRAN, M. S. & SCHUMACHER, J. 2012 Conditional statistics of thermal dissipation rate in turbulent Rayleigh–Bénard convection. *Eur. Phys. J.* E **35**, 108.

GROSSMANN, S. & LOHSE, D. 2000 Scaling in thermal convection: a unifying view. *J. Fluid Mech.* **407**, 27–56.

GROSSMANN, S. & LOHSE, D. 2001 Thermal convection for large Prandtl number. *Phys. Rev. Lett.* **86**, 3316–3319.

GROSSMANN, S. & LOHSE, D. 2004 Fluctuations in turbulent Rayleigh–Bénard convection: the role of plumes. *Phys. Fluids* **16**, 4462–4472.

GROSSMANN, S. & LOHSE, D. 2011 Multiple scaling in the ultimate regime of thermal convection. *Phys. Fluids* **23**, 045108.

HUANG, S.-D., KACZOROWSKI, M., NI, R. & XIA, K.-Q. 2013 Confinement induced heat transport enhancement in turbulent thermal convection. *Phys. Rev. Lett.* **111**, 104501.

HUNT, J. C. R., VRIELING, A. J., NIEUWSTADT, F. T. M. & FERNANDO, H. J. S. 2003 The influence of the thermal diffusivity of the lower boundary on eddy motion in convection. *J. Fluid Mech.* **491**, 183–205.

KACZOROWSKI, M. & WAGNER, C. 2009 Analysis of the thermal plumes in turbulent Rayleigh–Bénard convection based on well-resolved numerical simulations. *J. Fluid Mech.* **618**, 89–112.

KADANOFF, L. P. 2001 Turbulent heat flow: structures and scaling. *Phys. Today* **54** (8), 34–39.

KRAICHNAN, R. H. 1962 Turbulent thermal convection at arbitrary Prandtl number. *Phys. Fluids* **5**, 1374–1389.

LOHSE, D. & XIA, K. Q. 2010 Small-scale properties of turbulent Rayleigh–Bénard convection. *Annu. Rev. Fluid Mech.* **42**, 335–364.

OSTILLA-MÓNICO, R., VAN DER POEL, E. P., VERZICCO, R., GROSSMANN, S. & LOHSE, D. 2014 Boundary layer dynamics at the transition between the classical and the ultimate regime of Taylor–Couette flow. *Phys. Fluids* **26**, 015114.

PARODI, A., VON HARDENBERG, J., PASSONI, G., PROVENZALE, A. & SPIEGEL, E. A. 2004 Clustering of plumes in turbulent convection. *Phys. Rev. Lett.* **92**, 194503.

PUTHENVEETTIL, B. A. & ARAKERI, J. H. 2005 Plume structure in high-Rayleigh-number convection. *J. Fluid Mech.* **542**, 217–249.

SANO, M., WU, X. Z. & LIBCHABER, A. 1989 Turbulence in helium-gas free convection. *Phys. Rev. A* **40**, 6421–6430.

SHISHKINA, O. & WAGNER, C. 2008 Analysis of sheet like thermal plumes in turbulent Rayleigh–Bénard convection. *J. Fluid Mech.* **599**, 383–404.

SHRAIMAN, B. I. & SIGGIA, E. D. 1990 Heat transport in high-Rayleigh number convection. *Phys. Rev. A* **42**, 3650–3653.

SIGGIA, E. D. 1994 High Rayleigh number convection. *Annu. Rev. Fluid Mech.* **26**, 137–168.

STEVENS, R. J. A. M., LOHSE, D. & VERZICCO, R. 2011 Prandtl number dependence of heat transport in high Rayleigh number thermal convection. *J. Fluid Mech.* **688**, 31–43.

STEVENS, R. J. A. M., VAN DER POEL, E. P., GROSSMANN, S. & LOHSE, D. 2013 The unifying theory of scaling in thermal convection: the updated prefactors. *J. Fluid Mech.* **730**, 295–308.

SUGIYAMA, K., NI, R., STEVENS, R. J. A. M., CHAN, T. S., ZHOU, S.-Q., XI, H.-D., SUN, C., GROSSMANN, S., XIA, K.-Q. & LOHSE, D. 2010 Flow reversals in thermally driven turbulence. *Phys. Rev. Lett.* **105**, 034503.

TILGNER, A., BELMONTE, A. & LIBCHABER, A. 1993 Temperature and velocity profiles of turbulence convection in water. *Phys. Rev. E* **47**, R2253–R2256.

VERZICCO, R. & CAMUSSI, R. 1999 Prandtl number effects in convective turbulence. *J. Fluid Mech.* **383**, 55–73.

VERZICCO, R. & CAMUSSI, R. 2003 Numerical experiments on strongly turbulent thermal convection in a slender cylindrical cell. *J. Fluid Mech.* **477**, 19–49.

XI, H. D., LAM, S. & XIA, K.-Q. 2004 From laminar plumes to organized flows: the onset of large-scale circulation in turbulent thermal convection. *J. Fluid Mech.* **503**, 47–56.

ZHOU, Q., SUN, C. & XIA, K.-Q. 2007 Morphological evolution of thermal plumes in turbulent Rayleigh–Bénard convection. *Phys. Rev. Lett.* **98**, 074501.

ZHOU, Q. & XIA, K.-Q. 2010 Physical and geometrical properties of thermal plumes in turbulent Rayleigh–Bénard convection. *New J. Phys.* **12**, 075006.